IOP Publishing Nanotechnology
Nanotechnology 29 (2018) 015403 (12pp) https://doi.org/10.1088/1361-6528/aa9a96

Controllable nanoscale inverted pyramids for highly efficient quasi-omnidirectional crystalline silicon solar cells

Xu Haiyuan[1], Zhong Sihua[1], Zhuang Yufeng[1] and Shen Wenzhong[1,2]

[1] Institute of Solar Energy, and Key Laboratory of Artificial Structures and Quantum Control (Ministry of Education), School of Physics and Astronomy, Shanghai Jiao Tong University, Shanghai 200240, People's Republic of China
[2] Collaborative Innovation Center of Advanced Microstructures, Nanjing 210093, People's Republic of China

E-mail: wzshen@sjtu.edu.cn

Received 14 September 2017, revised 6 November 2017
Accepted for publication 14 November 2017
Published 4 December 2017

Abstract

Nanoscale inverted pyramid structures (NIPs) have always been regarded as one of the paramount light management schemes to achieve extraordinary performance in various devices, especially in solar cells, due to their outstanding antireflection ability with relative lower surface enhancement ratio. However, current approaches to fabricating NIPs are complicated and not cost-effective for massive cell production in the photovoltaic industry. Here, controllable NIPs are fabricated on crystalline silicon (c-Si) wafers by Ag-catalyzed chemical etching and alkaline modification, which is a preferable all-solution-processed method. Through applying the NIPs to c-Si solar cells and optimizing the cell design, we have successfully achieved highly efficient textured solar cells with NIPs of a champion efficiency of 20.5%. Significantly, these NIPs are further demonstrated to possess a quasi-omnidirectional property over broad sunlight incident angles of approximately 0°–60°. Moreover, NIPs are theoretically revealed to offer light trapping advantages for ultrathin c-Si solar cells. Hence, NIPs formed by a controllable method exhibit great potential to be used in the future photovoltaic industry as surface texture.

Supplementary material for this article is available online

Keywords: nanoscale inverted pyramids, high efficiency, quasi-omnidirectional, solar cells, light trapping

(Some figures may appear in colour only in the online journal)

1. Introduction

Inverted pyramid structures (IPs) have always been regarded as an important surface light management scheme to achieve extraordinary performance in various fields or devices, such as photonic crystals [1, 2], light emitting diodes [3, 4], solar cells [5–8] and so forth. Zhao *et al* [6] have demonstrated a world-record high efficiency (η) of 24.7% (25.0% after spectral rectification) in crystalline silicon (c-Si) homojunction solar cells with IPs texturization. Generally, for a light incident to the surface with micro-scale IPs, it is believed [8] that IPs can induce more multiple reflections between their exposed slope planes to effectively decrease the total reflection, and thus enhance the light absorption for solar cells. Multifarious surface structures, such as nanowires [9, 10] and nanoholes [11], have also been shown to possess an exceptional antireflection ability, and can be adopted in solar cells to increase optical gain. However, these nanostructures exhibit rather high surface enhancement ratio, which can lead to severe surface recombination, strong electrical loss and therefore unsatisfactory cell performance [10]. In contrast, IPs are more suitable for solar cells for both antireflection characteristics and lower surface enhancement ratio. The almost 1.7-fold surface enhancement ratio (compared to the planar

 © 2017 IOP Publishing Ltd Printed in the UK

surface) will alleviate the surface recombination, and can offer the convenience of obtaining a better surface passivation. These advantages are critical to realize highly efficient solar cells.

Hence the techniques to fabricate IPs have become a focus of research interest. There are many researchers demonstrating that IPs can be formed by hard-mask (e.g., dielectric mask or metal mask) assisted methods. For instance, Branham *et al* [7] and Zhou *et al* [12] have successfully fabricated IPs on c-Si substrates, respectively. However, the fabrication processes are very complicated, and involve depositing a nitride dielectric mask or sputtering a titanium layer to define etching patterns for the subsequent alkaline etching. A laser-assisted approach [13] would be an alternative method to obtain IPs, but there are disadvantages of laser induced surface damage of wafers and extra costs. These aforementioned methods are not convenient and cost-efficient, and therefore are not suitable for the low-cost requirement of the photovoltaic industry. Recently, researchers have reported that large-area IPs can be effectively formed on the surface of Si wafers by metal-assisted chemical etching [8, 14, 15], which is simple and compatible with the current production lines for solar cells. Yang *et al* [8] have fabricated 18.87% efficient c-Si solar cells based on IPs by a Cu assisted texturization technique. In addition, Jiang *et al* [15] have introduced a post acid rebuilding process with a 50 °C heated NaF/H_2O_2 mixed solution process to eventually obtain textured multi-crystalline silicon (mc-Si) solar cells based on IPs with *a* η of 18.62%. Obviously, there is still scope for improving the performance of silicon solar cells based on IPs and employing preferable nontoxic alkaline reagents commonly used in the photovoltaic industry.

However, Si nanostructures have been demonstrated to possess omnidirectional antireflection characteristics over a broad range of incident angles (θ) [16–18], which can bring great benefits for the application of solar cells since θ varies with time in a day and a year. We have recently confirmed that Si nanopyramids have a quasi-omnidirectional characteristic over θ of 0°–50° and can boost electric energy production with relative enhancement up to 2.5% [18]. Hence, it is highly motivating to fabricate a nanoscale IPs (NIPs) texture and explore the dependence of the electric energy production ability of the textured solar cells based on NIPs on θ. Moreover, it should be noted that NIPs also have the advantage for application in ultrathin c-Si solar cells due to their much smaller absorber loss and excellent light trapping effect [7, 12].

In this study, we have realized all-solution-processed NIPs on large-scale ($156 \times 156\,mm^2$) Si wafers by the combination of Ag-assisted chemical etching and alkaline modification. Through good control of the size of the NIPs, we have successfully achieved highly efficient textured c-Si solar cells based on NIPs with a champion η of 20.5%. The high η is ascribed to the superior antireflection properties and the extraordinary passivation effect provided by the NIPs' textured surfaces after coating with SiN_x/SiO_2 stack layers. Our textured solar cells based on NIPs have further demonstrated a quasi-omnidirectional property over the broad θs of approximately 0°–60°. In addition, we will show theoretically that our NIPs' textured surfaces could be utilized to realize excellent light trapping for ultrathin c-Si solar cells.

2. Experimental section

2.1. NIPs' texturization

Solar-grade boron-doped (100)-oriented Czochralski (CZ) crystalline silicon (c-Si) wafers (pseudo square $156 \times 156\,mm^2$, with resistivity of 1–3 $\Omega \cdot$ cm and thickness of $190 \pm 10\,\mu m$) were used as the substrates in our experiment. The wafers were etched in NaOH solution with a concentration of 10 wt.% at a temperature of 80 °C for about 3 min to remove the saw-damage layer and obtain a polished surface. Then, three crucial steps were conducted to form the NIPs' textured surface, as shown in figure 1(a). First, the polished substrates were immersed in a mixed solution of 0.1 mM $AgNO_3$ and 0.5 M HF for 30 s, which aimed to deposit a layer of randomly distributed Ag nanoparticles onto the polished surface (Step 1). Subsequently, the wafers deposited with Ag nanoparticles were dipped into a mixed solution of 1.5 M HF and 0.5 M H_2O_2, resulting in a Si nanoholes textured surface (Step 2). Finally, the nanohole structures were modified in NaOH solution with a concentration of 2 wt.% (Step 3). It should be noted that the c-Si wafers need to be immersed in a dilute HNO_3 solution (volume ratio 1:1 with deionized water) for 10 min before and after Step 3 to thoroughly remove the Ag particles, as confirmed by the energy-dispersive x-ray spectroscopy (EDX) in the supplementary information (figure S1 is available online at stacks.iop.org/NANO/29/015403/mmedia), and in the deionized water between every two steps mentioned above to remove the residual solution. All the procedures for the NIPs' texturization were carried out at room temperature.

2.2. Solar cell fabrication

Figure 1(b) presents the fabrication flow of the NIPs' textured solar cells. After all-solution-processed NIP texturization, rear surface polishing in an alkaline solution was carried out. Then, the SiO_2/SiN_x passivation layers were deposited on the rear surface of the NIPs' textured wafers by a plasma-enhanced chemical-vapor deposition (PECVD) process (CETC 48th Research Institute M82200-6/UM) at a temperature of 450 °C, utilizing the reactant gas sources N_2O/SiH_4 and NH_3/SiH_4 to produce SiO_2 (~25 nm) and SiN_x (~250 nm) layers with a deposition rate of ~5 nm min^{-1} (SiO_2) and ~9.5 nm min^{-1} (SiN_x), respectively. To engender the n^+ emitter, the textured c-Si wafers underwent a diffusion process with $POCl_3$ as the dopant source in a quartz-tube furnace (CETC 48th Research Institute M5111-4WL/UM) for 40 min at 800 °C. The emitter sheet resistance of the textured wafers after diffusion was about 90–100 $\Omega\ sq^{-1}$. A succeeding ablating procedure was executed by a laser (DR Laser DR-LA-Y40) to render local line openings with a width of 50 μm and a pitch of 1 mm. After removing the phosphorous silicate glass (PSG) in a dilute HF

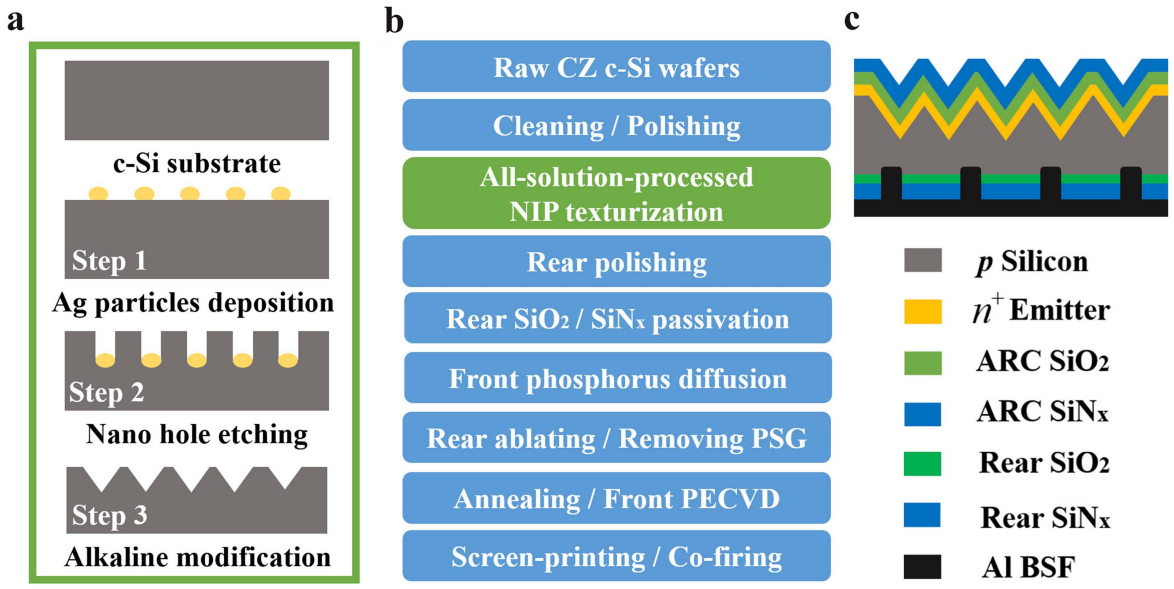

Figure 1. (a) Main steps of the NIPs' texturization processes. (b) Fabrication flow of the NIPs' textured solar cells. (c) Schematic diagram of the device structure of the NIPs' textured solar cells with the legends shown below.

solution, the NIPs samples were annealed at an optimal temperature of 725 °C for 60 min in an air atmosphere. Finally, the conformal stack SiO_2 (~5 nm)/SiN_x (~75 nm) layers were deposited on the front surface to serve as antireflection coatings (ARC) by PECVD at 400 °C, and commercially equipped screen-printing (DEK PV1200) and co-firing processes (Despatch CF Series) were performed successively to form the metal contacts and Al back surface field (BSF). Figure 1(c) schematically illustrates the cell structure without showing the electrodes.

2.3. Characterization

The morphologies of the NIPs were investigated by a field emission scanning electron microscope (Zeiss Ultra Plus). The size statistics, angle measuring and number counting of NIPs were assisted by the open-source software ImageJ. The reflectance spectra, together with the external quantum efficiency (*EQE*) and internal quantum efficiency (*IQE*) curves were measured via quantum efficiency measurement equipment (PV measurements QEX10). The electrical performance parameters of the solar cells were figured out by current–voltage (*I*–*V*) measurements (CETC 48th Research Institute Y05-1/UM) under the illumination of AM1.5G.

2.4. Finite difference time domain (FDTD) simulation

To investigate the omnidirectional characteristics of the NIPs' textured surfaces, about 30 NIPs of sizes between 630–860 nm were randomly distributed in a 4 μm × 4 μm square of a 2 μm-thick c-Si substrate in the *x*-*y* plane. Note that some NIPs were overlapped to mimic the experimental NIPs' textured surface, and two sample configurations were simulated without and with an 80 nm-thick SiN_x layer as the ARC (the SiO_2 layer has little influence on the simulation results because it is ultrathin). Bloch boundary conditions were adopted in the *x*-*y* plane because θ varies in the range of 0°–80°, and the boundary conditions in the *z* directions were set as perfectly matched layers. The light source was a plane wave with a fixed wavelength of 800 nm for that the non-normal incidence exists. To obtain the surface reflectance, a power monitor was set above the light source. For mapping the electric intensity distribution with different θs, a NIPs unit with an opening size of 750 nm was modeled on the c-Si substrate, changing θ from 0° to 80°.

To explore the light trapping effect of the NIPs' textured surfaces for ultrathin c-Si solar cells, the NIPs' textured surfaces were modeled onto a 5 μm-thick c-Si substrate in the *x*-*y* plane, together with a planar counterpart and NIP-750 nm counterpart for comparison. In the NIP-B scenario, approximately 30 NIPs of sizes between 630–860 nm were randomly distributed in a 4 μm × 4 μm square of the c-Si substrate with periodic boundary conditions. Also, some NIPs were partly overlapped with each other, which is in accordance with the surface of the experimentally fabricated NIP-B sample. In the NIP-750nm scenario, the opening size of the NIPs was set as 750 nm with a separation width of 100 nm and 4 × 4 arrays were used in the *x*-*y* plane with periodic boundary conditions. All the front surfaces (planar, NIP-750 nm and NIP-B surfaces) were covered with an 80 nm-thick SiN_x layer, while all the rear sides of the ultrathin c-Si substrates were covered with a 100 nm-thick SiN_x layer (inner) and 200 nm-thick Ag layer (outer). The plane wave light source with wavelength changing from 400 to 1200 nm was propagating downwards (normally incident to the planar surface). The top and bottom boundary conditions of the *z*-axis direction are a perfectly matched layer and metal layer, respectively. A power monitor was placed above the light source (parallel to the *x*-*y* plane) to obtain the reflectance (*R*), and an absorption monitor was used to obtain the absorption within the Ag layer (A_{Ag}). The light absorption in the ultrathin c-Si substrates could therefore be calculated as 1-*R*-A_{Ag}. To reveal the light trapping effects

within the Si bulk, another power monitor was positioned in the x-z plane to obtain the distribution of electric field intensity.

In the simulation, all the NIPs were set as regular ones with an angle of 54°, which is the characteristic angle between the Si (111) facet and (100) facet. The optical constants were directly extracted from the material database, except for the refractive index of SiN_x, which was fixed at a constant value of 2 without considering the extinction coefficient. All the simulations above were performed using a commercial software package (Lumerical FDTD Solutions 2017a).

3. Results and discussion

3.1. Controllable formation and mechanism of the NIPs' morphology

To obtain insight into the evolution of surface morphologies and reveal the formation mechanism, systematic investigations of each step of the NIPs' texturization have been performed. As depicted in figure 1(a), our texturization method mainly consisted of three critical steps: Ag particles deposition (Step 1), Ag-catalyzed nanohole etching (Step 2) and alkaline modifying (Step 3). In our etching system, the reaction in Step 1 could be described as the electroless deposition of Ag nanoparticles:

$$Ag^{+} + Si_{VB} + HF \rightarrow Ag\,(s) + H_2SiF_6 + H^{+}. \quad (1)$$

In the reaction of equation (1), Ag ions inject the hole (h^{+}) to the valence band of silicon and thus are reduced, resulting in the oxidation of Si atoms beneath Ag nanoparticles. The Si oxides are removed by HF in the solution, and thus Ag nanoparticles can adhere to the Si surface. The solution with ultralow Ag^{+} concentration of 0.1 mM was utilized, and a layer of well-dispersed Ag nanoparticles could then be spread onto the surface of the polished c-Si wafers in Step 1. Figures 2(a), (b) present the Ag nanoparticles randomly distributed on the surface of a polished c-Si substrate with sizes of about 10–25 nm; their interspaces are mainly in the range of 40–120 nm with a mean interspace of ~76 nm. Compared with the Ag nanoparticles self-assembled by the solid-state dewetting method [29], the size and interspaces of the Ag nanoparticles observed in our experiment are smaller overall, although they are both randomly distributed.

Figure 2(c) shows the cross-sectional SEM image of the as-etched sample for 20 min in a mixed solution of HF/H_2O_2 in Step 2. The down-straight aligned nanoholes can be obviously observed, with the porous surface shown in the inset. Nanoholes were formed via the catalyzed electrochemical reactions beneath the Ag particles in Step 2:

$$Si + HF + H_2O_2 \xrightarrow{Ag} H_2SiF_6 + H_2O + H_2(g). \quad (2)$$

It is well accepted that the reactions of equation (2) include the cathode reactions at the metal and anode reactions at the etching front, as illustrated in figure 2(g). The cathode reactions mainly indicate that H_2O_2 was reduced into H_2O, and the charge transfer process (the h^{+} injection from H_2O_2 into c-Si substrate) was accelerated by the sinking Ag particles. The anode reactions are about the ways in which silicon atoms catch h^{+} to be oxidized and dissolved. In fact, the first two steps are the representative processes of the metal catalyzed chemical etching method; some detailed reaction models can be found in previous studies [19, 20]. The Si atoms beneath the Ag particles were eliminated faster than a surface without deposited Ag particles, hence the nanoholes can be naturally dug out. Note that the concentration of etchants greatly affects not only the etching rate, but also the etched surface structures in this process. Chartier *et al* [20] investigated the dependence of etched silicon structures on the ratio parameter ρ (defined as $\rho = [HF] / ([HF] + [H_2O_2])$), and experimentally confirmed that Ag particles dug vertically into the surface of Si wafers and produced nanoholes analogous to a straight cylinder when ρ was above 70%. In our HF (1.5 M)/H_2O_2 (0.5 M) etching system, ρ is calculated to be 75%, enabling and ensuring the straight aligned nanoholes formed in Step 2, which is a prerequisite for the formation of NIPs.

After etching for 5 min in Step 3, the nanoholes change a lot, as illustrated in figure 2(d). The nanoholes enlarge into the composite structure with diamond-shaped openings, and amazingly, the facets of Si (111) began to show up with the bottom IPs having an opening size of ~200 nm, as shown in the inset. The sidewall had a length of ~1.3 μm, and exhibited smooth flanks. When the etching time was prolonged to 10 min, the opening size of the bottom IPs widened to ~400 nm, but the length of sidewall shortened to ~600 nm, as shown in figure 2(e). Figure 2(f) demonstrates the top-view surface of the sample modified for 10 min in Step 3. Similar to figure 2(e), it can be seen that the composite structures were randomly located, and the sidewall was eliminated to render more slope facets of Si (111). In addition, it could be observed that partial Ag particles in the inset of figure 2(f) (solid circles) were embedded in the focus of the bottom IPs. These Ag nanoparticles have acted as the catalyzed etching front in Step 2, and been retained at the bottom of the nanoholes (without the process of dilute HNO_3); in contrast to that some Ag dendrites (dash circles) were located in the inferior textured areas lacking IPs. The composite structures would become more regular IPs on condition that the etching time in Step 3 was adequate and proper to remove the sidewalls completely. The gradual transformation from nanoholes to NIPs was attributed to the anisotropic etching of silicon in alkaline solution:

$$Si + OH^{-} + H_2O \rightarrow SiO_3^{2-} + H_2\,(g). \quad (3)$$

The etching rate of equation (3) differs for different crystallographic planes [21], as depicted in figure 2(h). The etching rate of Si (111) planes in alkaline solution is the lowest, therefore the NIPs could be eventually obtained.

3.2. Different NIPs' textured surfaces with successively modulated opening size distribution

Considering the NIPs' formation mechanism described above, it naturally occurred to us that the opening size of the

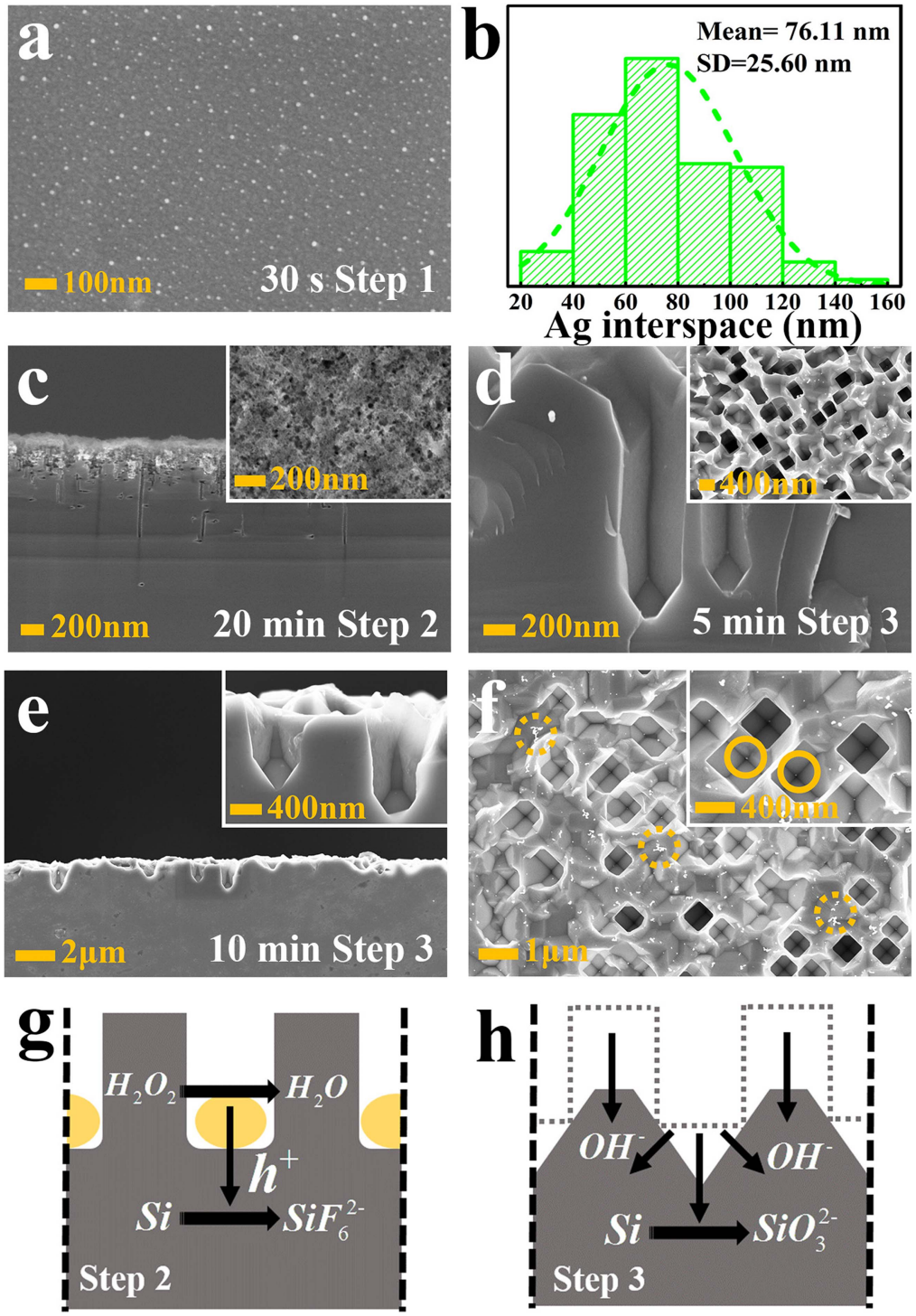

Figure 2. (a) Top-view SEM image of the 30-s-deposited Ag nanoparticles on the surface of polished c-Si substrates. (b) Statistical diagram of the Ag nanoparticles interspace distribution with the mean interspace and standard deviation (SD) manifested. (c) Cross-sectional SEM image of a 20 min-etched c-Si substrate in Step 2 with the inset showing a top-view of the porous surface. (d) Cross-sectional image of the 5 min-modified sample in Step 3 after a 20 min-etching in Step 2. The inset shows the top-view surface. The cross-sectional (e) and top-view (f) SEM image of the as-modified sample (without removing Ag particles in the dilute HNO_3 solution) with the etching time in Step 3 prolonged to 10 min. The insets are close-ups of the features in the corresponding surface. Schematic diagrams of the ideal etching scenario for (g) nanoholes unit formed in Step 2 and (h) NIPs unit in Step 3, respectively.

NIPs can be manipulated by adjusting the processing time in Step 2 and Step 3. As listed in table 1, three groups of NIPs' textured samples (NIP-A, NIP-B and NIP-C) were prepared by varying the etching time in Step 2 and Step 3. The deposition time in Step 1 was fixed at 30 s to render similar initial coverage of Ag nanoparticles on the wafers, as shown in figure 2(a). The nanoholes formed in Step 2 with an etching time of 20 min were converted into composite structures

Table 1. Different texturization recipes with the processing time varied to successively modulate the opening size distribution of the NIPs.

Group	Step 1 [s]	Step 2 [min]	Step 3 [min]
NIP-A	30	20	13
NIP-B	30	30	18
NIP-C	30	40	23

when anisotropically etched in NaOH solution, as shown in figures 2(d)–(f). When modified for 13 min in Step 3, as illustrated in figure 3(a1) for the NIP-A sample, the sidewalls of the composite structures are mostly eliminated and NIPs are uniformly and compactly cover the surface of c-Si wafers. As more clearly displayed in the inset, some of them were even interconnected or overlapped with each other. The cross-sectional SEM of figure 3(a2) also confirms that the fabricated structures are mainly NIPs-like. To ascertain the dimension of the opening sizes of the NIPs, a statistical opening size distribution were attained via measuring and counting the NIPs' units from figure 3(a1). As shown in figure 3(a3), NIP-A have opening sizes distributed from 300 to 800 nm, which can be well fitted by the normal distribution function (red line) with the mean of 453.16 nm and standard deviation (SD) of 63.69 nm.

We had extended the ething time of Step 2 to 30 and 40 min to yield the precursors of the NIP-B and NIP-C samples, respectively. Owing to that, the catalyzed etching was at a stable rate of approximately 107 nm min^{-1}; the longer the etching time in Step 2, the deeper the nanoholes became, and thus the more modification time it cost in Step 3 to form the overall enlarged NIPs' units. Therefore, the modification times of 18 and 23 min in Step 3 were respectively required for NIP-B and NIP-C to sufficiently trim the sidewalls away and to form the enlarged NIPs, as shown in figure 3(b1, b2, c1 and c2). Figure 3(b3) shows that the opening sizes of NIP-B are distributed from 500 to 1100 nm, which can also be perfectly fitted by the normal distribution function (orange line). For NIP-C, we have further successfully enhanced the opening size to principally 730–1160 nm, as presented in figure 3(c3). Therefore, by increasing the etching time in Step 2 to acquire deeper nanoholes and correspondingly costing more modification time in Step 3, successive modulation of the opening size distribution of the NIPs' textured surface had been realized. Moreover, it should be noted that the method to form the NIPs' texture is an all-solution-processed method, which is more cost-effective than present popular techniques to construct IPs' architectures.

Concerning the optical performance, as illustrated in figure 3(d), reflectance spectra are presented in a wavelength ranging from 400 to 1200 nm for the NIP-A, NIP-B and NIP-C textured surfaces, respectively. It can be obviously found that all the textured wafers possess a similar tendency of reflectance characteristics since their surfaces are all covered by the NIPs. Nevertheless, it appears that the NIP-A textured surface can provide a lower level of reflectance with an average reflectance (R_{ave}) of 13.0% than the R_{ave}s of NIP-B (14.1%) and NIP-C (15.7%) textured surfaces. Here, the R_{ave} is calculated by weighing the reflectance over a broad wavelength range of 400–1200 nm of the standard AM1.5G spectrum as in the following equation:

$$R_{ave} = \frac{\int_{400\,nm}^{1200\,nm} R(\lambda) \cdot S(\lambda) \cdot d\lambda}{\int_{400\,nm}^{1200\,nm} S(\lambda) \cdot d\lambda} \quad (4)$$

where $R(\lambda)$ is the experimental reflectance depending on λ (the wavelength) and $S(\lambda)$ represents the standard AM1.5G solar photon flux spectral distribution. The slight incremental alteration of R_{ave}s can be attributed to fact that the flat fraction separating the NIPs on the wafer surface was gradually raised while prolonging the etching time in Step 2 and Step 3 to form the expanded NIP-B and NIP-C texture as shown in figure 3. For the reflectance measuring, we have further investigated the varying positions on the large-scale NIPs' textured wafers ($156 \times 156\,mm^2$). In figure 3(e), the reflectance spectra of the NIP-B textured surface demonstrate that different positions of the c-Si wafer have a nearly identical reflectance over the whole wavelength range of 400–1200 nm, which manifests the homogeneous texture of the surfaces with NIPs. Generally, the IP-like surfaces appeared to exhibit different antireflection performance for the distinct textured wafers obtained by different methods, which is related to the specific IPs' shapes. For micon-scale IPs reported by Yang *et al* [8], and Wang *et al* [14], a mean reflectance down to ~4% is revealed. However, the R_{ave}s for our NIPs' textured wafers are overall lower than that of the IPs with a scale of 300–700 nm fabricated on mc-Si wafers [15]. In addition, our NIPs' textured wafers demonstrate a similar reflectance level to the semi-periodic micon-scale IPs, which have been perfectly modified by the subsequent 4 min KOH processing of the laser-assisted method [13].

3.3. Performance analysis of the NIPs' textured c-Si solar cells

For solar cells, performance lies not just in the low reflectance, but also in the trade-off of advantages in optical and electrical aspects. When the NIPs' textured wafers have been coated with SiN_x/SiO_2 stack layers as the ARC (without considering the refractive index gradient of the ultrathin SiO_2 layer used), the difference of their reflectance (dash lines in figure 4(a)) diminished, resulting in similar R_{ave}s (5.25%, 5.27% and 6.00% for NIP-A, NIP-B and NIP-C, respectively). The experimental *EQE* of the NIPs' textured c-Si solar cells (solid lines in figure 4(a)), are almost overlaid except that the NIP-C textured solar cells have lower values in the wavelength range of 400–600 nm. This is coincident with the measured reflectance characteristics of the NIP-C textured surface with ARC because it possesses a slightly higher reflectance in the short wavelength region, which can be attributed to the fact that the planar fraction of the NIP-C textured surface was a little higher to induce slightly thicker front stack layers. When it comes to the *IQE* which evaluates the collection capacity of the absorbed incident photons, three NIPs' textured solar cells reveal the commensurate level as shown in figure 4(b). This indicates the similar efficient collection nature of the different NIP-A, NIP-B and NIP-C textured solar cells.

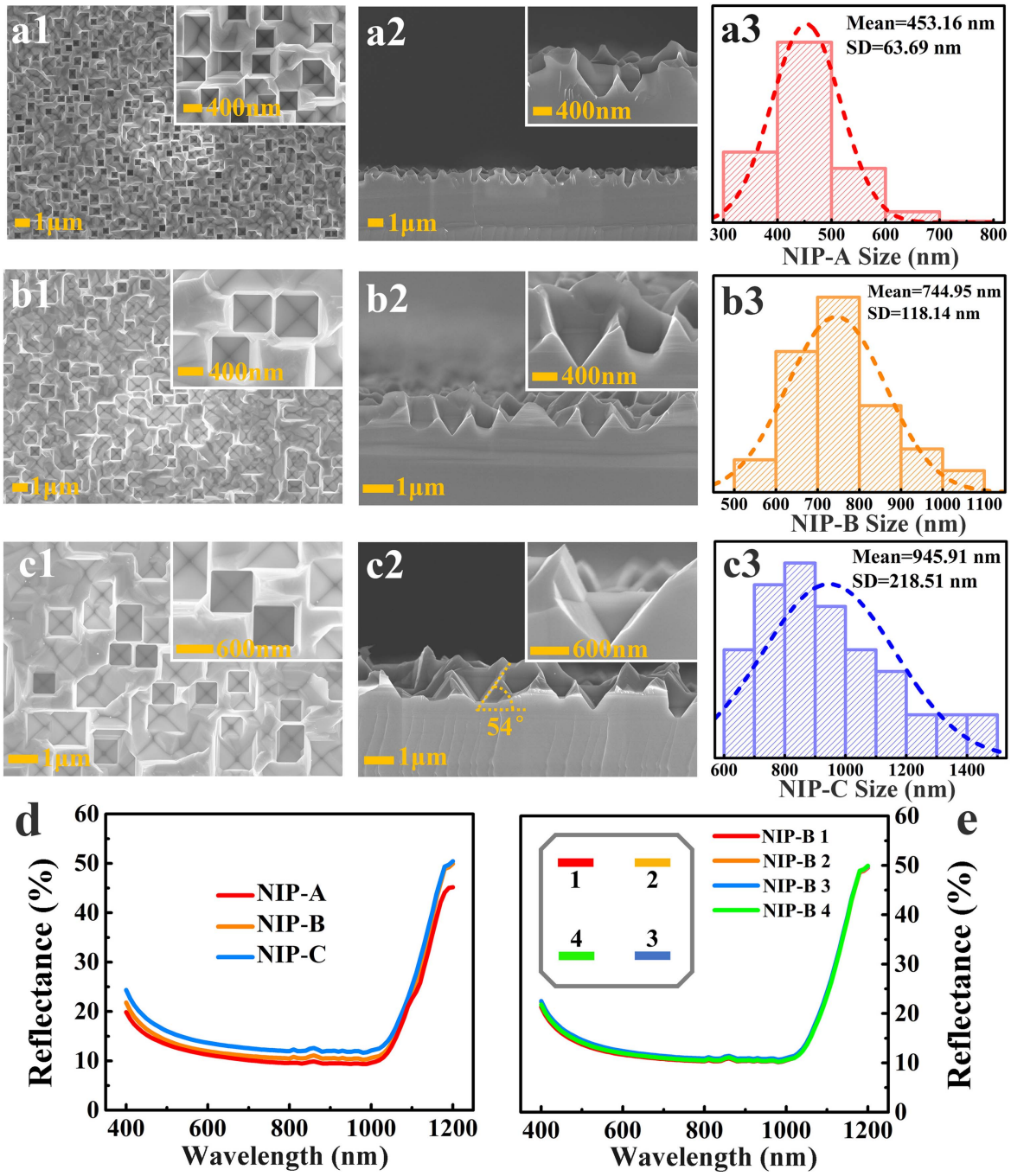

Figure 3. Top-view (a1, b1 and c1) and cross-sectional (a2, b2 and c2) SEM images of the as-textured samples under a different texturization recipe in table 1 as NIP-A, NIP-B and NIP-C, respectively. The insets show the corresponding zoomed-in view of the NIPs. The statistical diagrams of the opening size distributions for the as-textured samples are illustrated in a3, b3 and c3, respectively, with the mean and SD manifested. (d) Reflectance spectra of the NIP-A, NIP-B and NIP-C as-textured wafer surfaces in the wavelength range of 400–1200 nm. (e) Reflectance spectra of the different positions on a large-size NIP-B as-textured wafer surface (quasi 156 × 156 mm^2). Numbers in the inset schematically indicate the measuring positions.

To analyze the comprehensive influence of the NIPs on cell performance, we illustrate the measured output electrical parameters in figures 4(c)–(f), which includes the short circuit current density (J_{SC}), open circuit voltage (V_{OC}), fill factor (*FF*) and η. The NIP-A, NIP-B and NIP-C textured solar cells have an average J_{SC}s of 39.2 mA cm^{-2}, 39.1 mA cm^{-2} and 38.9 mA cm^{-2}, respectively. They all acquire exceptional average J_{SC}s owing to the great antireflection abilities of their NIPs' surfaces, and the variation of J_{SC}s is inkeeping with the R_{ave}s. The ARC-coated NIP-A and NIP-B textured wafers have a similarly lower R_{ave}s than that of the NIP-C samples, and thus their J_{SC}s are higher. As shown in figure 4(d), the V_{OC}s of the NIPs' textured solar cells are rather high and retain nearly the same extent with the discrepancy restricted in 1 mV. This can be ascribed to the fact that the NIP-A, NIP-B and NIP-C textured wafers have a similar and rather low

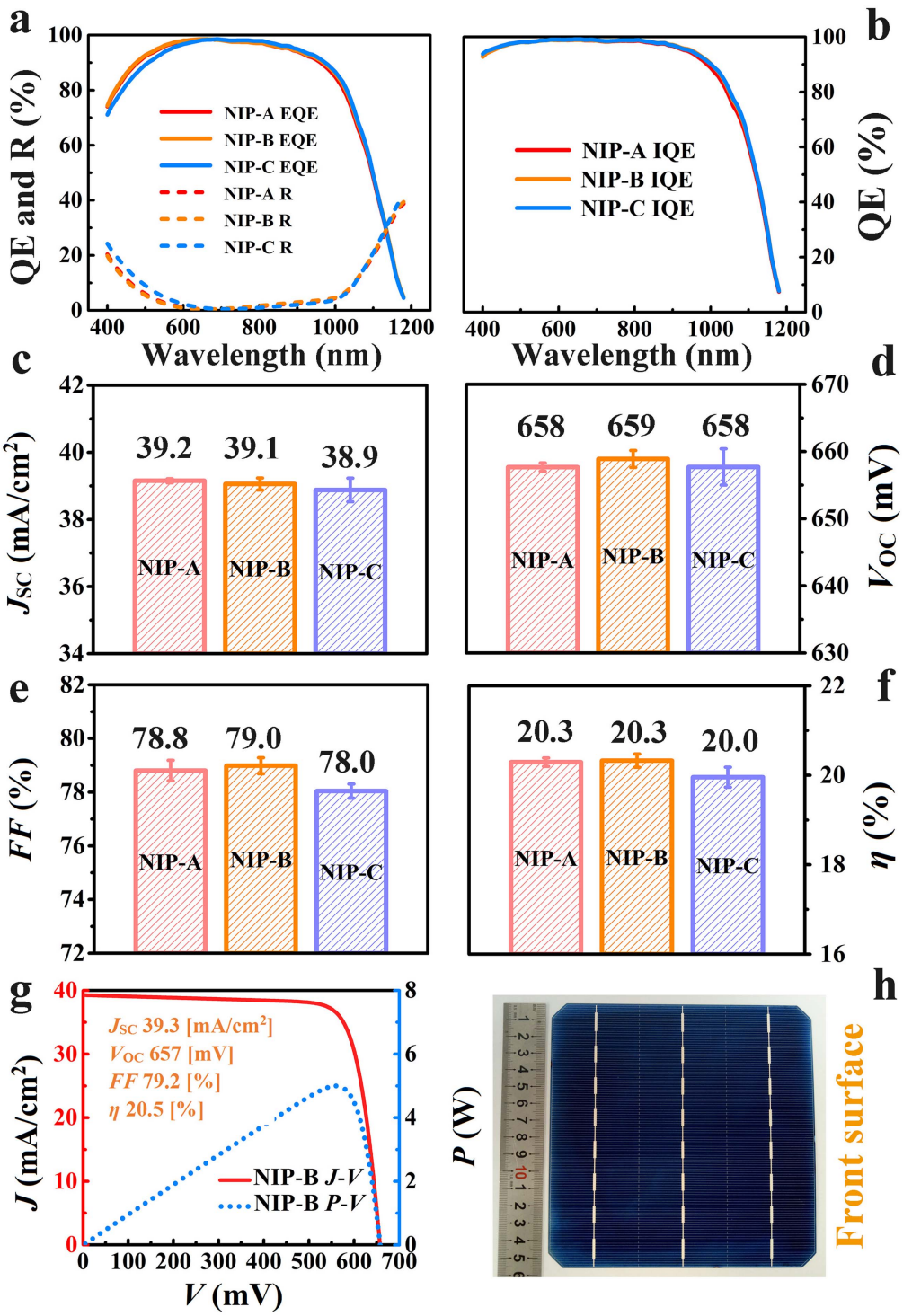

Figure 4. (a) Experimental *EQE* (solid lines) of the NIP-A, NIP-B and NIP-C textured c-Si solar cells, together with the reflectance spectra (dash lines) of the corresponding NIPs' textured wafers coated with SiN_x/SiO_2 stack layers as the ARC. (b) Experimental *IQE* characteristics of the different NIPs' textured c-Si solar cells. The average performance parameters: (c) J_{SC}, (d) V_{OC}, (e) *FF* and (f) η of the NIP-A, NIP-B and NIP-C textured c-Si solar cells, respectively. (g) *J–V* and *P–V* characteristics of the best NIP-B textured solar cell. (h) Digital photograph of the best NIP-B textured solar cell showing the front dark-blue surface.

surface enhancement. Moreover, the double-sided stack SiO_2/SiN_x layers contribute to the excellent surface passivation effect. Our group [22] have previously confirmed that optimally annealed stack SiO_2/SiN_x layers could bring about an ultra-low surface recombination velocity of 18.3 cm s^{-1}, benefiting from the formation of more Si-O and Si-H bonds to suppress the dangling bonds in the Si/SiO_2 interface. In this study, we have also carried out the same optimal annealing process for the stack SiO_2/SiN_x layers to guarantee an excellent surface passivation effect and optical response (see

supplementary information, figure S2) with an optimal rear stack layer thickness of ~25 nm and ~250 nm, respectively.

According to the measured J_{SC}s and V_{OC}s, we have evaluated the total diode saturating current density J_0 as the following equation:

$$J_0 = J_{SC} \Big/ \left[\exp\left(\frac{qV_{OC}}{kT}\right) - 1\right]. \quad (5)$$

In equation (5), T is the absolute temperature and kT/q denotes the thermal voltage (25.7 mV at 25 °C). The J_0 are obtained as the values of 299.2 fA cm^{-2}, 284.7 fA cm^{-2} and 296.8 fA cm^{-2} for the NIP-A, NIP-B and NIP-C textured solar cells, respectively. The J_0 of the present NIPs' textured solar cells are obviously at a similar level and are lower than that (357.15 fA cm^{-2}) of the c-Si nanowires/micro-pyramids based solar cell with the same device framework [22], which implies a reduced recombination loss of the n^+ emitter including the Auger and surface recombination for the smaller surface area enhancement ratio of NIPs.

Figure 4(e) shows the *FF*s of the NIPs' textured solar cells, and it turns out that the NIP-A and NIP-B solar cells possess generally higher average *FF*s. Resulting from the optical gain and electrical amelioration, all the NIP textured solar cells exhibit high average ηs as displayed in figure 4(f). In particular, it should be mentioned that NIP-A and NIP-B textured solar cells can offer superior ηs (20.3%) than that (20.0%) of NIP-C textured solar cells owing to their preferable J_{SC}s and *FF*s. Figure 4(g) presents the *J*–*V* (red solid line) and *P*–*V* (blue dot line) characteristics of the best NIP-B textured solar cell. The highest η reached 20.5%, and the maximum output power of 5.0 W was realized on the quasi-square wafers with a size of 244.3 cm^2. We have also provided in figure 4(h) the digital photograph of the best NIP-B textured solar cell to show that the whole front surface exhibits the uniform color of dark blue, which is favorable for the mass production of the photovoltaic industry. The above results demonstrate that it is apparently feasible to incorporate the NIPs' surface texturization by our all-solution-processed method (Ag-assisted etching and alkaline modifying process) into the current solar cell production lines. Besides, considering that the current technical routines have not fully been optimized for the fabrication of NIPs' based solar cells, the performance (particularly the η) can be further improved by optimizing the procedures.

3.4. Quasi-omnidirectional characteristics of the NIPs' textured solar cells

When looking at our finished NIPs' textured solar cells, it is interesting to find that they always appear to be dark-blue regardless of whether they are observed from the top view or tilted view, which suggests that the NIPs' textures have an omnidirectional antireflection ability. We have investigated the dependence of the reflectance of the NIPs' textured surfaces on θ by FDTD simulation. Figure 5(a) shows the simulated configurations for the NIPs' textured surfaces without and with the ARC (for simplicity, just the NIP-B textured surface and the ARC of SiN_x layer with thickness of 80 nm). The definition of θ is also provided by the red arrow in figure 5(a), which represents the angle between the incident light and the normal to the NIPs' textured surface. As illustrated in figure 5(b), the simulated surface reflectance of the as-textured and coated NIP-B samples at 800 nm manifests nearly the same tendency with the changing θs. The reflectance of the as-textured NIP-B sample (red line) ascends very slowly with increasing θ in the range of 0°–50°. However, the reflectance begins to increase rapidly when θ goes beyond 60°. The reflectance of the NIP-B sample with the ARC (blue line) is largely reduced to be lower than 5% with θ between 0°–50°, and it is (coincidentally) the same as that of the as-textured one in rising dramatically when θ is larger than 60°. For our NIPs' textured samples, the changing states of the surface reflectance is very similar to the reported results of other Si nanostructures [16–18], which have already proved to possess omnidirectional characteristics and be capable of generating more electricity while harvesting solar energy in the non-normal incidence occasions of sunlight. Hence, the advantage of our NIPs can be more prominent for antireflection in the occasions of non-normal incidence.

To further confirm the quasi-omnidirectional electric energy production ability of the NIPs' textured solar cells, we have experimentally measured their *EQE*s at the wavelength of 800 nm with the θ changing from 0° to 70°, as shown in figure 5(c). It can be seen that the *EQE* of the NIP-B textured solar cells declines slightly and maintains a high level of >90% over the broad θs of 0°–60°. Nevertheless, the *EQE* decreases sharply when θ is over 60° and it can be obviously ascribed to the swift enhancement of the surface reflectance with θ beyond 60° as observed in figure 5(b). To explore the coupling effect of the incident light with our NIP-B textured surface, we have also performed a numerical simulation to map the electric field intensity distribution beneath a NIPs' unit with an opening size of 750 nm under different θs. As displayed in figure 5(d), it can be obviously found that the electric field intensity remains strong until θ exceeds 60°. This can be attributed to the fact that the incident light couples well with the NIPs through light scattering and localized optical resonances when θ ranges from 0°–60°, which provides the benefit to significantly reduce the surface reflectance. However, the optical resonances diminish markedly when θ increases to 70° and 80°, and this leads to a dramatic increase of the surface reflectance. Therefore, the quasi-omnidirectional antireflection ability and thus the similar *EQE* performance fundamentally come from effective light coupling into the NIPs' textured solar cells over broad θs. It can be expected that the quasi-omnidirectional *EQE* performance of the NIPs' textured solar cells will generate high electric energy in a day and in a year.

3.5. Simulated light trapping advantage of the NIPs for ultrathin c-Si solar cells

One of the paramount applications of NIPs is to serve as an excellent light trapping solution to obtain better performance

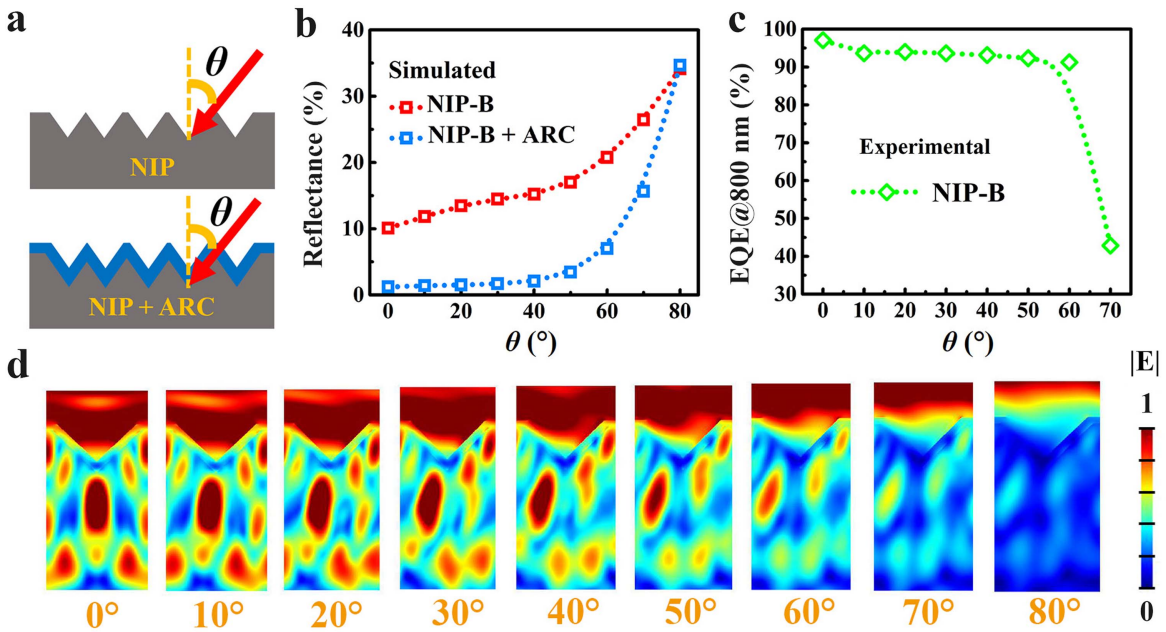

Figure 5. (a) Simulated sample configurations for the NIP-B textured surface without and with the 80 nm-thick SiN_x layer as the ARC. (b) Simulated reflectance of NIP-B textured surface versus θ with and without the ARC. (c) Experimental *EQE* values of NIP-B textured solar cells at an incident light wavelength of 800 nm with varying θs of 0°–70°. (d) Electric field intensity mapping within the c-Si substrate beneath the single NIP unit with an opening size of 750 nm for the different θs.

in ultrathin c-Si solar cells [7, 23]. It is revealed in our experiment that the bulk material loss on each wafer side is about 2–5 μm in the texturing process to form the NIPs, which is much less than the generally etched thickness of 5–10 μm in the alkaline solution for micro-pyramids texturing [24]. Hence, it is important to utilize NIPs' texture into ultrathin c-Si solar cells with a device thickness of tens of microns.

In order to understand the light trapping advantage of our NIPs' textured surfaces (simply taking the NIP-B as the representative), we employed a FDTD simulation to obtain and compare the light absorption of different samples. The thickness of the modeled c-Si substrates is 5 μm. In the NIP-B scenario, the opening sizes of the NIPs are arranged as the values extracted randomly from the normal distribution curve of the NIP-B textured surface as illustrated in figure 3(b3). The positions of NIPs are disorderly located on the substrate surface to resemble those of the experimentally fabricated structures. Additionally, two counterparts with a planar surface and periodic NIP arrays (noted as the NIP-750 nm sample) were also simulated for comparison, respectively. In the NIP-750 nm scenario, the opening size of the NIPs is set as 750 nm that approaches the mean size of the NIP-B sample. Figure 6(a) shows the simulation configurations for the planar, NIP-750 nm and NIP-B samples. All the simulated c-Si substrates are sandwiched by a front SiN_x layer (80 nm in thickness) and rear SiN_x layer (100 nm in thickness), together with a 200 nm-thick rear outer-coated Ag reflector. Figure 6(b) presents the simulated absorption spectra of all the samples. It can be seen that the planar counterpart (grey line) has high absorption only in the vicinity wavelength of 600 nm. In contrast, the simulated NIP-750 nm counterpart (blue line) possesses high absorption generally over a broad wavelength ranging from 400 to 1200 nm. For the NIP-B sample (red line), its absorption curve manifests a similar tendency over the wide spectrum range to that of the NIP-750 nm counterpart. In particular, the absorption curve of the NIP-B sample appears to be commensurate with that of the NIP-750 nm counterpart in the short wavelength range, but exceeds that in the long wavelength except for some oscillation peaks of the NIP-750 nm counterpart. It is revealed that the light trapping ability of the NIP-B textured surface rivals or is even better than that of the NIP periodic arrays surface with similar opening sizes. It is well-known that the most popular techniques to form well-defined NIP arrays are inevitably involved with complicated procedures to make the etching patterns [7]. Excitingly, our NIP texturization method is much easier and more cost-effective, but is also able to provide superior light trapping properties.

Figure 6 further shows the electric field intensity distributions of the simulated planar counterpart (figures 6(c1)–(c3)), NIP-750 nm counterpart (figures 6(d1)–(d3)) and the NIP-B sample (figures 6(e1)–(e3)) under the incident light wavelength of 457, 640 and 1091 nm, respectively. At a short wavelength region (457 nm) it can be obviously found that more light has entered into the NIP-B sample in figure 6(e1). The interference from the SiNx layer of the planar configuration resulted in reflecting much incident light back into the air, but the NIPs could induce the localized Mie resonance channel for incident light. The electric field intensity distribution of the NIP-B sample in figure 6(e2) and planar counterpart in figure 6(c2) seems to be conspicuously different at the middle wavelength region (640 nm), although they both possess high absorption. It shows that the

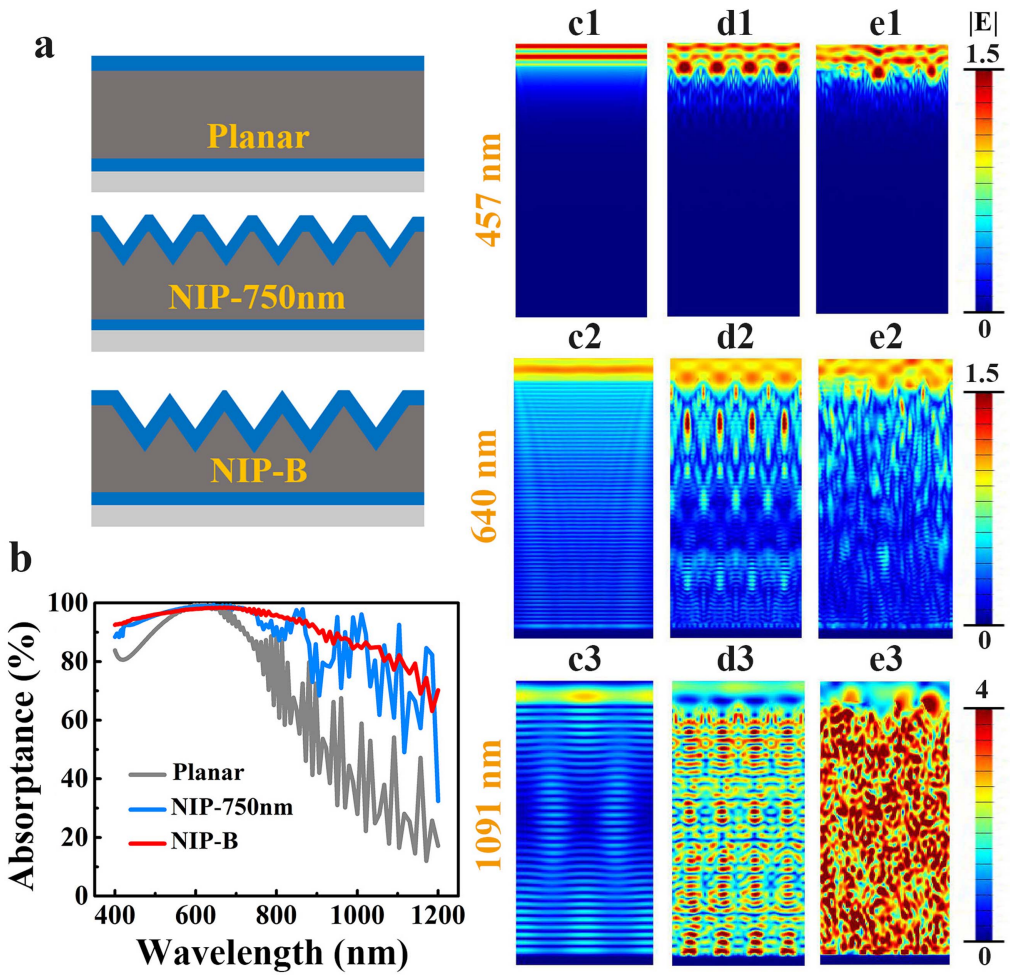

Figure 6. (a) Simulated sample configurations for the planar, NIP-750nm and NIP-B textured surfaces, respectively. (b) Simulated absorption spectra of the planar counterpart, NIP-750 nm counterpart and NIP-B sample. The electric field intensity distributions of the planar counterpart (c1, c2 and c3), NIP-750 nm counterpart (d1, d2 and d3) and NIP-B sample (e1, e2 and e3) are displayed corresponding to the incident light wavelength of 457, 640 and 1091 nm, respectively.

interference and Fabry–Perot resonance emerge in the planar configuration, while the localized Mie resonance and Fabry–Perot resonance as well as the guided resonance are excited in the NIP-B sample [24, 25]. At the long wavelength region (1091 nm), figure 6(c3) indicates that the Fabry–Perot resonance is retained but the destructive interference is reduced. In contrast, the NIP-B textured surface still leads to a strong electric field distribution by exciting multiple optical resonances, as shown in figure 6(e3), and thus achieves higher absorption characteristics. When compared with the electric field intensity distribution of the NIP-750 nm counterpart in figures 6(d1)–(d3), our NIP-B sample tends to excite distorted multiple resonances with spatially enlarged distributions. It is attributed to the fact that the NIPs with normally distributed opening sizes and random positions can offer stronger effects of forward light scattering and resonances, which have already been revealed for some nanostructures with disordered morphologies [24, 26–28]. In addition, it can also be noted that the NIP-750 nm counterpart has an impressible dependence on the wavelength and its light absorption fluctuates due to the periodic NIP arrays, especially in the long wavelength range. For our NIP-B sample, the light absorption is promoted evenly over the wide spectrum, and thus its resonant electric field intensity is more prominent (except for the wavelength inducing the high oscillation peaks of the absorption curve for the NIP-750 nm counterpart). Therefore, our NIPs are believed to offer an exceptional light trapping advantage over the broad wavelength range.

4. Conclusions

In conclusion, we have successfully fabricated NIPs as the surface texture for large-size ($156 \times 156\,mm^2$) c-Si solar cells. The mean opening sizes of NIPs are easily modulated by adjusting the etching time in the Ag-catalyzed chemical etching and alkaline modification processes, which is an all-solution-processed method that is convenient and cost effective. Benefiting from superior antireflection properties and a good passivation effect provided by the SiN_x/SiO_2 stack layers coated NIPs, highly efficient c-Si solar cells with an average η of 20.3% are successfully obtained. In particular, the best NIPs' textured solar cells demonstrate a high J_{SC} of $39.3\,mA\,cm^{-2}$ and the highest η of 20.5%, as well as a

maximum output power of 5.0 W on quasi-square wafers with a size of 244.3 cm^2. Furthermore, the *EQE* values of the optimal NIPs' textured solar cells maintain a high level of >90% (at the wavelength of 800 nm) over broad θs of 0°–60°, owing to the exceptional quasi-omnidirectional antireflection characteristics of the NIPs. Therefore, NIPs' textured c-Si solar cells are a type of quasi-omnidirectional solar cells, which are believed to be capable of boosting electricity production in a day and in a year. Last, but not least, by the FDTD simulation, our NIPs are demonstrated to offer an exceptional light trapping advantage for ultrathin c-Si solar cells as their light absorption are commensurate with, and even rival, similar periodic NIP counterparts.

Acknowledgments

This work was supported by the Natural Science Foundation of China (61234005, 11474201 and 11674225), and China Postdoctoral Science Foundation (15Z102060052 and 16Z102060054).

ORCID iDs

Xu Haiyuan https://orcid.org/0000-0003-1117-915X

References

[1] Sergey E, Sajeev J, Hafez M, Al-Ameer S S, Al-Harby T S, Al-Hadeethi Y and Bouwes D M 2015 *J. Appl. Phys.* **118** 023103
[2] Chen Z-H, Qiao N, Wang Y, Liang L, Yang Y B, Ye H and Liu S D 2016 *Appl. Energy* **172** 59–65
[3] Krames M R *et al* 1999 *Appl. Phys. Lett.* **75** 2365–7
[4] Kuo C H, Chang L C, Kuo C W and Tun C J 2009 *J. Electrochem. Soc.* **156** H986–9
[5] Shi D, Zeng Y and Shen W Z 2015 *Sci. Rep.* **5** 16504
[6] Zhao J H, Wang A H and Green M A 1999 *Prog. Photovoltaics Res. Appl.* **7** 471–4
[7] Branham M S, Hsu W-C, Yerci S, Loomis J, Boriskina S V, Hoard B R, Han S E and Chen G 2015 *Adv. Mater.* **27** 2182–8
[8] Yang L X, Liu Y P, Wang Y, Chen W, Chen Q S, Wu J T, Kuznetsov A and Du X L 2017 *Sol. Energy Mater. Sol. Cells* **166** 121–6
[9] Huang Z G, Lin X X, Zeng Y, Zhong S H, Song X M, Liu C, Yuan X and Shen W Z 2015 *Sol. Energy Mater. Sol. Cells* **143** 302–10
[10] Zhong S H, Huang Z G, Lin X X, Zeng Y, Ma Y C and Shen W Z 2015 *Adv. Mater.* **27** 555–61
[11] Peng K-Q, Wang X, Li L, Wu X-L and Lee S-T 2010 *J. Am. Chem. Soc.* **132** 6872–3
[12] Zhou S Q, Yang Z H, Gao P Q, Li X F, Yang X, Wang D, He J, Ying Z Q and Ye J C 2016 *Nanoscale Res. Lett.* **11** 194
[13] Yang B and Lee M 2014 *Opt. Laser Technol.* **63** 120–4
[14] Wang Y, Yang L X, Liu Y P, Mei Z X, Chen W, Li J Q, Liang H L, Kuznetsov A and Du X L 2015 *Sci. Rep.* **5** 10843
[15] Jiang Y, Shen H L, Pu T, Zheng C F, Tang Q T, Gao K, Wu J, Rui C B, Li Y F and Liu Y W 2017 *Sol. Energy* **142** 91–6
[16] Spinelli P, Verschuuren M A and Polman A 2012 *Nat. Commun.* **3** 692
[17] Savin H, Repo P, von Gastrow G, Ortega P, Calle E, Garín M and Alcubilla R 2015 *Nat. Nanotechnol.* **10** 624–8
[18] Zhong S H, Wang W J, Tan M, Zhuang Y F and Shen W Z 2017 *Adv. Sci.* **4** 1700200
[19] Huang Z P, Geyer N, Werner P, de Boor J and Gösele U 2011 *Adv. Mater.* **23** 285–308
[20] Chartier C, Bastide S and Lévy-Clément C 2008 *Electrochim. Acta* **53** 5509–16
[21] Zhou Z F, Huang Q A and Li W H 2009 *J. Electrochem. Soc.* **156** F29–37
[22] Huang Z G, Song X M, Zhong S H, Xu H Y, Luo W X, Zhu X D and Shen W Z 2016 *Adv. Funct. Mater.* **26** 1892–8
[23] Mavrokefalos A, Han S E, Yerci S, Branham M S and Chen G 2012 *Nano Lett.* **12** 2792–6
[24] Zhong S H, Wang W J, Zhuang Y F, Huang Z G and Shen W Z 2016 *Adv. Funct. Mater.* **26** 4768–77
[25] Brongersma M L, Cui Y and Fan S H 2014 *Nat. Mater.* **13** 451–60
[26] Sturmberg B C P, Dossou K B, Botten L C, Asatryan A A, Poulton C G, McPhedran R C and de Sterke C M 2012 *Appl. Phys. Lett.* **101** 173902
[27] Vynck K, Burresi M, Riboli F and Wiersma D S 2012 *Nat. Mater.* **11** 1017–22
[28] Trompoukis C, Massiot I, Depauw V, Daif O E, Lee K D, Dmitriev A, Gordon I, Mertens R and Poortmans J 2016 *Opt. Express* **24** A191–201
[29] Araújo A, Mendes M J, Mateus T, Vicente A, Nunes D, Calmeiro T, Fortunato E, Aguas H and Martins R 2016 *J. Phys. Chem.* C **120** 18235–42